ISBN: 978-628-96613-3-0. ISSN: 2414-6390. Digital Object Identifier: https://dx.doi.org/10.18687/LACCEI2026.1.1.2634

Physics-Informed 3D Simulation and Data Architecture for AI-Driven Magnetic Micro-robots in Endovascular Navigation

Amelia Fernández Seguel[1]
Faculty Mentor: Alejandro I. Maass[1]
[1]Pontificia Universidad Católica de Chile, Chile
afernandezs3@estudiante.uc.cl, alejandro.maass@uc.cl

***Abstract*—Achieving precise navigation within the human circulatory system requires a robust understanding of the complex micro-scale forces at play. This paper presents a comprehensive theoretical and computational framework for the navigation of a composite magnetic micro-robot, composed of a ferromagnetic-polymer matrix, within a 3D vascular environment. The mathematical model integrates magnetic gradient actuation, non-linear hydrodynamic drag, apparent weight, and short-range forces, including electrostatic interactions and Hertzian contact mechanics. Crucially, to bridge the gap between biomechanical simulation and Artificial Intelligence, the physics-informed MATLAB environment was equipped with a high-frequency data extraction architecture. This system dynamically records teleoperated navigation as Markov Decision Process (MDP) tuples (S_t, A_t, R_t), using a dense reward function that heavily penalizes simulated tissue collisions. Results demonstrate not only the feasibility of navigating against dynamic hemodynamic conditions using multi-axial magnetic gradients, but also the successful generation of high-fidelity datasets. This provides a robust, pre-computed foundation for training autonomous medical interventions via Offline Reinforcement Learning, paving the way for safer and more accessible endovascular therapies.**

Keywords–Microrobotics, Magnetic Actuation, MATLAB Simulation, Hemodynamics, Reinforcement Learning

I. Introduction

Robotics has transformed many scientific fields, particularly medicine, where it has aided in enhanced diagnosis and treatment by enabling greater precision and reduced invasiveness [1]. While macroscopic systems, like robotic arms, are now widely used in operating rooms, the next frontier lies in the development of submillimetric devices capable of navigating wirelessly the human body, accessing hard-to-reach cavities. These micro-robotic systems hold the potential to revolutionize procedures that currently require highly invasive interventions [2].

A primary challenge in medical micro-robotics is achieving precise, wireless movement within dynamic physiological environments, such as the circulatory system. In these scenarios, micro-robots must navigate against pulsatile blood flow and avoid collisions with vascular walls or cellular components to reach specific targets, such as arterial occlusions. Since usual components, such as microcontrollers, sensors and motors, can not be used in this scale, magnetic control has emerged as a leading solution due to its safety, ability to generate 3D forces, and deep penetration into biological tissues without causing physical damage. [3].

Recent research has explored the use of micro-robotic capsules, often integrating ferromagnetic nanoparticles within a polymeric gelatin hydrogel matrices to combine structural integrity with magnetic responsiveness. For instance, advanced systems using zinc-doped iron oxide and tantalum nanoparticles have demonstrated visibility under X-ray fluoroscopy and the ability to be controlled by flow gradients [4]. Such devices enable “active thrombolysis,” which a robot delivers a concentrated therapeutic payload (such as tissue plasminogen activator) directly to a clot, minimizing the systemic side effects and drug dilution associated to traditional intravenous treatments [5].

Despite these physical advances, autonomous clinical application requires robust computational frameworks [6]. Precise control and future AI-driven autonomy depend on an accurate understanding of the forces governing micro-scale motion, including hydrodynamic drag, magnetic gradients, and contact mechanics.

This work presents a comprehensive mathematical description of the forces acting on a magnetically actuated micro-robot within a vascular environment. This theoretical framework was integrated into a physics-informed 3D simulation environment developed in MATLAB. The simulation features a pulsatile blood flow model, interactive real-time control, and a contact model to account for vessel wall interactions. This environment serves as a foundation for the future design of complex controllers and autonomous navigation algorithms.

II. Theoretical Framework

A. Actuation Principle

The micro-robot studied consists of a spheric composite material: ferromagnetic particles embedded within a polymer matrix. The magnetic particles enable the micro-robot to interact with applied external fields, while the polymer binds these particles together and provides the necessary buoyancy and structural integrity. [7] During the fabrication process, the ferromagnetic particles are aligned using a strong magnetic field before the polymer is cured. This ensures that the magnetic moments of all particles share a common orientation.

Since the particles are uniformly aligned, the entire micro-robot can be modelled as a single magnetic dipole. Consequently, the magnetic force $\vec{F}_m$ applied to the robot is described by:

$$\vec{F}_m = (\vec{m} \cdot \nabla)\vec{B} \tag{1}$$

where $\vec{m}$ is the magnetic moment and $\vec{B}$ is the magnetic field. Instantaneous magnetic alignment with the external field is assumed due to the micro-robot's small rotational inertia.

III. Mathematical Modelling

A. Main Equation

The motion of the micro-robot is governed by Newton's Second Law:

$$\vec{F} = m \cdot \vec{a} \tag{2}$$

Adapting this to the specific forces acting on the system, the equation of motion becomes:

$$\sum \vec{F} = m\frac{d\vec{v}}{dt} = \vec{F}_m + \vec{F}_d + \vec{W}_a \tag{3}$$

where $\vec{W}_a$ and m the apparent weight and the mass of the micro-robot respectively, $\vec{F}_m$ the magnetic force and $\vec{F}_d$ the hydrodynamic drag force.

B. Hydrodynamic Force

This component describes the drag force exerted by the fluid on the submerged micro-robot, representing the resistance to motion caused by the fluid viscosity and density.

To derive this component, we considered the dynamic pressure acting on the body. Starting from the concept of kinetic energy (E_k) using mass and simple velocity (v):

$$E_k = \frac{1}{2}mv^2 \tag{4}$$

Expressing this in terms of fluid density (ρ_f) rather than mass per unit volume, we obtain the dynamic pressure (p_q):

$$\frac{E_k}{Vol} = \frac{1}{2}\rho_f v^2 = p_q \tag{5}$$

The drag force is proportional to this dynamic pressure acting over a specific reference area. Since pressure acts against the direction of motion, the projected frontal area of the micro-robot is used, defined as $A = \pi r^2$, where r is the sphere radius:

$$F \propto \left(\frac{1}{2}\rho_f A v^2\right) \tag{6}$$

To account for the shape of the object and the flow characteristics, a dimensionless coefficient known as the drag coefficient (C_d) is introduced.

$$F = \frac{1}{2}\rho_f A C_d v^2 \tag{7}$$

Finally, to incorporate this magnitude into the vector equation of motion, directionality was added. The force acts in opposition to the velocity vector:

$$\vec{v} \to -\frac{\vec{v}}{||\vec{v}||} \tag{8}$$

Since the micro-robot navigates within a moving fluid, the force depends on the relative velocity between the robot ($\vec{v}$) and the fluid ($\vec{v}_f$). Additionally, a wall-effect correction factor (β) is included to account for the increased resistance when navigating narrow channels (such as arteries).

Incorporating these terms, the final expression for the hydrodynamic drag force is:

$$\vec{F}_d = -\frac{1}{2}\rho_f A C_d \left(\frac{||\vec{v} - \vec{v}_f||}{\beta}\right)^2 \frac{(\vec{v} - \vec{v}_f)}{||\vec{v} - \vec{v}_f||} \tag{9}$$

This equation encapsulates the force direction, fluid density, relative velocity magnitude, geometry, and flow conditions.

C. Apparent Weight

This term represents the net vertical force acting on the micro-robot, accounting for both gravitational attraction and the opposing buoyant force (Archimedes' principle).

Starting from the definition of weight:

$$\vec{W} = m\vec{g} = V\rho\vec{g} \tag{10}$$

Since the micro-robot is submerged, the density difference between the robot and the fluid must be considered to obtain the apparent weight $\vec{W}_a$:

$$\vec{W}_a = V(\rho - \rho_f)\vec{g} \tag{11}$$

where $\vec{g}$ is the acceleration due to gravity, ρ_f corresponds to the fluid density (which may be a scalar constant or a time-varying function), and ρ is the effective density of the micro-robot. This is determined by the rule of mixtures:

$$\rho = \tau_m \rho_m + (1 - \tau_m)\rho_{poly} \tag{12}$$

This calculation considers the ferromagnetic ratio τ_m, the density of the magnetic material ρ_m, and the density of the polymer matrix ρ_{poly}. The ferromagnetic ratio is defined as the volume fraction of magnetic material: $\tau_m = \frac{V_m}{V}$.

D. Magnetic Force

This component corresponds to the translational force exerted by the external magnetic field on the micro-robot. It is important to distinguish that a uniform magnetic field $\vec{B}$ generates torque (rotating the dipole), whereas the magnetic gradient $\nabla\vec{B}$ generates the translational force responsible for locomotion. The force is given by:

$$\vec{F}_m = \tau_m V(\vec{M}\cdot\nabla)\vec{B} \tag{13}$$

where $\tau_m V$ represents the effective volume of the magnetic material within the sphere of volume $V = \frac{4}{3}\pi r^3$. Expanding the gradient operator ∇ and the dot product $(\vec{M}\cdot\nabla)$, the force vector can be expressed in matrix form as:

$$\begin{bmatrix} F_x \\ F_y \\ F_z \end{bmatrix} = \tau_m V \begin{bmatrix} \frac{\partial B_x}{\partial x} & \frac{\partial B_y}{\partial x} & \frac{\partial B_z}{\partial x} \\ \frac{\partial B_x}{\partial y} & \frac{\partial B_y}{\partial y} & \frac{\partial B_z}{\partial y} \\ \frac{\partial B_x}{\partial z} & \frac{\partial B_y}{\partial z} & \frac{\partial B_z}{\partial z} \end{bmatrix}^T \begin{bmatrix} M_x \\ M_y \\ M_z \end{bmatrix} \tag{14}$$

where the matrix represents the spatial gradients of the magnetic field (the control inputs), the vector $\vec{M}$ represents the robot's magnetization orientation, and x, y, z represents the three spatial dimensions.

Assuming the rotational inertia is negligible, the robot aligns instantaneously with the primary field direction. If we consider the primary field aligns the robot with the Z-axis (or the gradient direction), the expression simplifies for simulation purposes to:

$$\vec{F}_m = (\tau_m V M_{sat})\cdot\nabla\vec{B}_{applied} \tag{15}$$

This simplified form allows the separation of the robot's magnetic capacity ($\tau_m V M_{sat}$) from the external control input ($\nabla\vec{B}$).

E. Electrostatic Force

This force describes the interaction between the electric charge of the micro-robot and the blood vessel walls, which are considered an uncharged surface. It is a short-range force that becomes relevant when hydrodynamic forces decreases.

To derive this component, Coulomb's law is considered:

$$F = \frac{1}{4\pi\epsilon\epsilon_0}\frac{q_1 q_2}{d^2} \tag{16}$$

with ϵ being the medium dielectric density and ϵ_0 the vacuum permittivity.

When a charge is close to a neutral force, polarization effects generate a net attractive force.

With this consideration, the blood vessel wall is replaced by an image charge of equal magnitude and opposite sign ($-q$ charge for a q charged robot).

The distance between the centre of the micro-robot and the wall is defined as:

$$h = r + \delta \tag{17}$$

where r corresponds to the micro-robot radius and δ is the distance between the surface of the micro-robot and the blood vessel wall.

When the wall effect depends on the gap distance to the nearest boundary, numerical issues may arise if the distance tends to zero (terms proportional to $1/\delta$). To avoid divergence, an effective distance is defined using a Heaviside step function (H):

$$\tilde{\delta}(\delta) = H(\delta)\,\delta + \big(1 - H(\delta)\big)\,r \tag{18}$$

with

$$H(\delta) = \begin{cases} 1, & \delta > 0 \\ 0, & \delta \le 0 \end{cases} \tag{19}$$

Thus, if $\delta > 0$ (no contact), the real distance is used ($\tilde{\delta} = \delta$); if $\delta \le 0$ (contact), the distance is saturated at the robot radius ($\tilde{\delta} = r$), preventing the model from tending to infinity.

Applied to Coulomb's formula, the resulting electric force is:

$$F_{el} = \frac{q^2}{4\pi\epsilon\epsilon_0}\cdot\left(\frac{H(\delta)}{(r+\delta)^2} + \frac{H(-\delta)}{r^2}\right) \tag{20}$$

F. Contact Force

To accurately simulate the interaction between the magnetic micro-robot and the arterial walls, a contact force model based on Hertzian theory is implemented. This model accounts for the mechanical response of the biological tissue during collision and the subsequent energy dissipation.

1) Loading Phase: Hertzian Contact: When the micro-robot impacts the arterial wall (approximated as an elastic plane), the initial compressive force follows the Hertzian Contact Theory. The loading force $\vec{F}_{load}$ is defined as:

$$\vec{F}_{load} = \frac{4}{3}E^*\sqrt{r}\delta^{3/2}\vec{n} \tag{21}$$

where δ represents the penetration depth (indentation), $\vec{n}$ is the normal unit vector at the contact point, and $H(\cdot)$ is the Heaviside step function, which ensures the force is only active during physical contact ($\delta < 0$). The contact stiffness K aggregates the geometric and material properties:

$$K = \frac{4}{3}E^*\sqrt{r} \tag{22}$$

Here, E^* is the effective Young's modulus, calculated from the elastic moduli (E) and Poisson's ratios (ν) of both the micro-robot (r) and the arterial wall (w)

$$\frac{1}{E^*} = \frac{1-\nu_r^2}{E_r} + \frac{1-\nu_w^2}{E_w} \tag{23}$$

2) Unloading Phase: Hysteresis and Dissipation: To account for the energy lost during the impact an unloading model is used. When the micro-robot bounces back, the force follows a different path:

$$\vec{F}_{unload} = -F\delta_m \left| \frac{\delta - \delta_0}{\delta_m - \delta_0} \right|^p H(-\delta)\vec{n} \tag{24}$$

In this expression, $F_{\delta m}$ is the maximum force reached at the point of maximum indentation δ_m. The parameter δ_0 represents the permanent deformation (or the point where the contact is broken during recovery), and the exponent p determines the curvature of the unloading path, dictating the rate of energy restoration.

3) Integrated Contact Law: The complete contact dynamics is governed by the following piecewise relationship:

$$\vec{F}_c(\delta) = \begin{cases} -K\,|\delta|^{3/2}\,H(-\delta)\,\vec{n}, & \text{loading} \\ -F_{\delta_m} \left| \dfrac{\delta - \delta_0}{\delta_m - \delta_0} \right|^p H(-\delta)\,\vec{n}, & \text{unloading} \end{cases} \tag{25}$$

G. Simulation Model Note: Hybrid Drag

Although the hydrodynamic force derived in Section III-B describes the drag behaviour primarily for higher velocities (Newtonian drag), numerical simulations can exhibit instability near zero velocity due to the quadratic nature of the term ($v^2 \to 0$).

To address this and to better represent the physics at the micro-scale where the Reynolds number is low ($Re \ll 1$), a linear Stokes drag term is superposed in the simulation model. This hybrid approach ensures numerical stability during hovering and slow manoeuvres, while maintaining the saturation effects of quadratic drag at higher velocities.

IV. Physical Implementation and State of the Art

The physical realization of magnetic navigation systems requires high-precision electromagnetic control to manage the micro-robot's position within a physiological workspace. Following the methodology proposed by [4], a configuration of six electromagnetic coils can be utilized to generate three-dimensional heterogeneous gradients within a 20x20x20 cm volume.

This setup is capable of producing magnetic gradients of up to 1 T/m, providing the necessary force to counteract gravitational effects and enable controlled locomotion against high-velocity blood flows.

The micro-robots described in this framework are composed of a thermosensitive gelatin hydrogel matrix. To enable magnetic actuation, zinc-doped iron oxide nanoparticles are embedded within the hydrogel. Additionally, tantalum nanoparticles are integrated into the structure to serve as radiopaque contrast agents, ensuring the robot can be accurately detected and tracked via X-ray fluoroscopy [4].

V. MATLAB implementation

A. Numerical Integration

A Runge-Kutta (RK4) integration scheme was chosen, which allows solving the system of ordinary differential equations (ODEs) of the robot dynamics. A pulsatile flow model was incorporated to simulate the real hemodynamic conditions in an artery of 3 mm diameter.

A cylindrical geometry was used as an initial approximation. Building upon this proof of concept, ongoing work has already extended this simulation to incorporate complex arterial anatomies (e.g., bifurcations and curvatures). The flow model was represented as:

$$v_f(t) = v_{mean} + v_{pulse} \cdot \sin(2\pi \cdot f_{cardiac} \cdot t)$$

Where v_{mean} represents the baseline mean velocity of the blood flow, v_{pulse} is the amplitude of the pulsatile velocity component, $f_{cardiac}$ denotes the cardiac frequency in beats per second, and t indicates the instantaneous simulation time. This model assumes a uniform velocity profile across the arterial lumen, simplifying the initial computational complexity. However, real arterial flow exhibits a parabolic (Poiseuille) profile, where velocity significantly decreases near the walls. Since the micro-robot navigates near the boundaries in several scenarios, this uniform assumption may overestimate the near-wall drag. Future iterations will incorporate Poiseuille and Womersley flow profiles to improve boundary navigation accuracy.

B. Control Panel and Visualization Interface

A five-component interactive panel was developed to enable real-time visualization and precise control over the micro-robotic agent. The interface is structured as follows:

- **A. 3D Navigation Workspace:** The upper section of the interface renders a 3D visualization of the cylindrical arterial lumen. This simulated environment displays the micro-robot (rendered in green) alongside dynamic obstacles representing red blood cells (rendered in red). In the absence of external magnetic actuation, the system visually demonstrates the passive transport of the agent driven by the local fluid velocity, while continuously tracing the robot's historical trajectory (blue path). The assigned target is constantly displayed (rendered in yellow)
- **B. Hemodynamic Monitor:** A real-time plot displaying the blood flow velocity. This graph captures the sinusoidal nature of the pulsatile flow previously explained.
- **C. Magnetic Gradient Controller:** This module displays the active gradients applied to the system. This movement is achieved through keyboard interrupts: the left and right arrows control the X-axis, up and down arrows manage the Y-axis, and the 'W' and 'S' keys modulate the Z-axis.

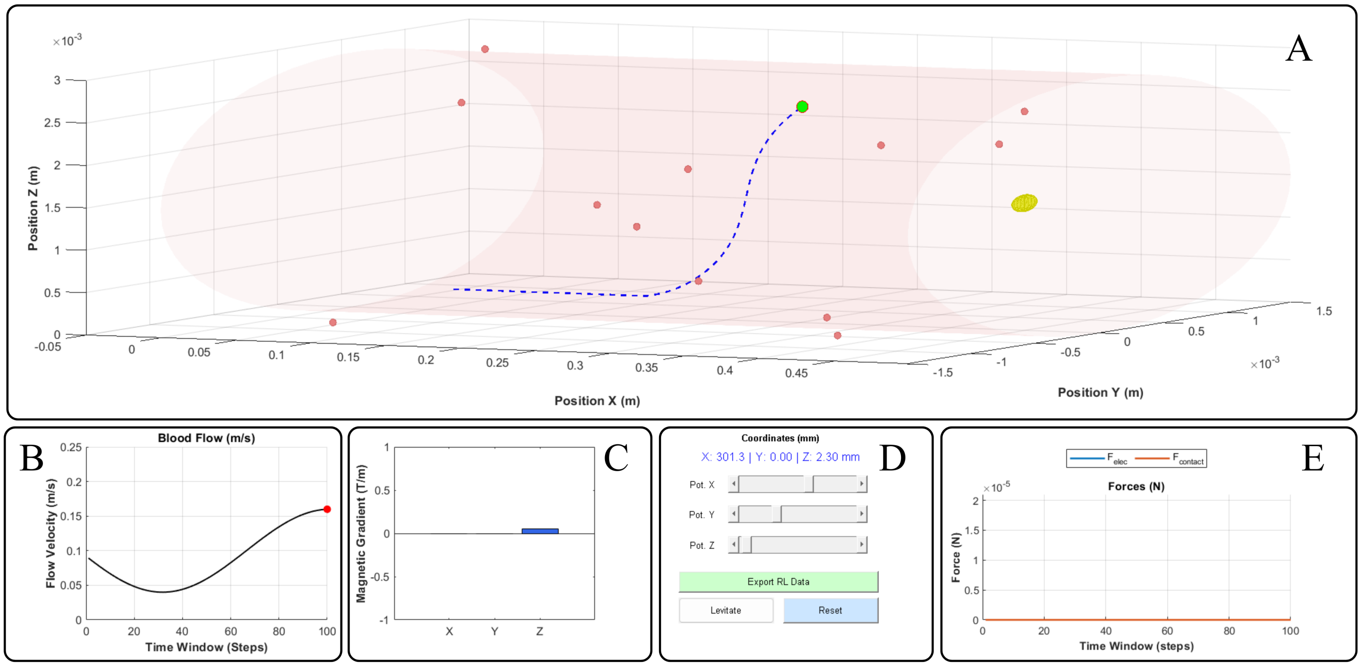

Fig. 1: Control Panel and Visualization Interface

- **D. Simulation Utilities:** Sliders are included to adjust the sensitivity and magnitude of these inputs dynamically. The system incorporates a "Levitation" toggle to automatically compensate for gravity, allowing for isolated analysis of planar movement. Additionally, a "Reset" function is provided to return the micro-robot to its initial coordinates.
- **E. Force Diagnostic Plot:** A dedicated graph monitors the electrostatic and contact forces acting upon the robot as it nears or impacts the vessel walls

This interface can be seen in Fig. 1.

C. Experimental Demonstration and Scenario Analysis

To validate the mathematical model and the simulation's responsiveness, four distinct navigation scenarios were evaluated. In all cases, the micro-robot's behaviour was recorded in response to varying magnetic gradients and physiological conditions.

1) **Passive Transport:** In the absence of external magnetic gradients, the micro-robot is subject only to hydrodynamic drag and gravity. As shown in Fig. 2a, the agent is dragged downstream by the pulsatile blood flow. Simultaneously, the lack of vertical compensation leads to gravitational sedimentation, resulting in a constant contact force against the lower arterial wall.
2) **Upstream Navigation (X-axis):** A negative magnetic gradient is applied to counteract the hydrodynamic drag force. As shown in Fig. 2b, the micro-robot demonstrates the ability to navigate against the flow. During this manoeuvre, the interaction with the vessel floor persists, maintaining the contact force seen.
3) **Vertical Levitation (Z-axis):** A gradient exceeding the apparent weight of the robot is applied. Fig. 2c shows the agent reaching the upper section of the vessel. It is observed that by modulating the gradient to nearly cancel out gravitational effects, the contact force is significantly reduced compared to the sedimentation scenario.
4) **Lateral Displacement and Complex Manoeuvring:** Fig. 2d and Fig. 2e demonstrate movement along the Y-axis and combined multi-axial trajectories, respectively. By mixing gradients, the micro-robot can perform complex 3D manoeuvre, avoiding obstacles and maintaining a stable trajectory, even under the influence of the pulsatile flow cycle.

For enhanced clarity, the user interface (UI) components have been omitted from Fig. 2, and the graphical markers for both the trajectory lines and obstacles have been scaled up for improved visualization.

D. Parameters

The physical and numerical constants used to ground the simulation are detailed in Table I. These values correspond to established biological and material data for magnetic micro-robots in endovascular environments.

E. Reinforcement Learning Integration

A primary challenge in developing AI-driven autonomy for micro-robotics is the computational bottleneck of training Deep Reinforcement (DRL) agents directly within high-fidelity physical environments. To ease its way, the simulation framework was equipped with a real-time data extraction architecture operating at a sampling frequency of 5 kHz,

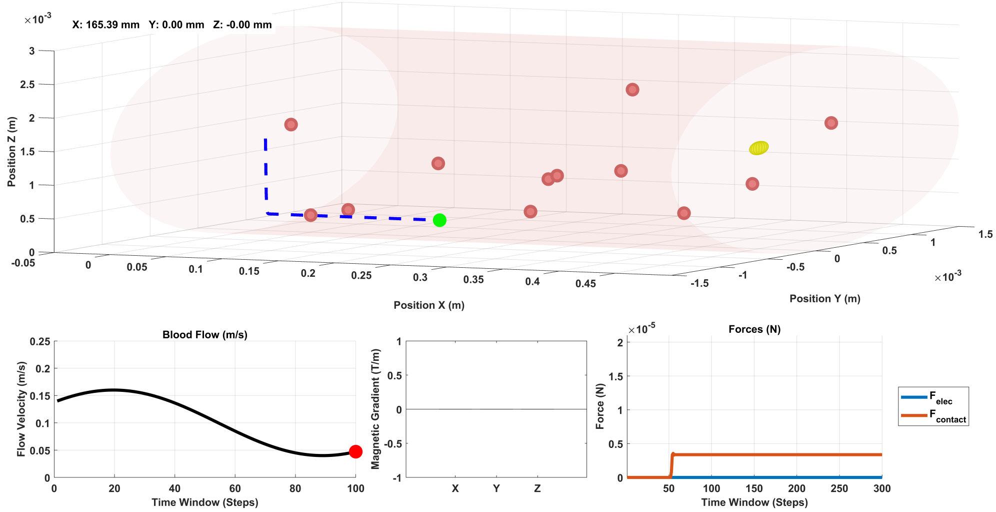

(a) Passive transport and gravitational sedimentation under pulsatile flow without magnetic actuation.

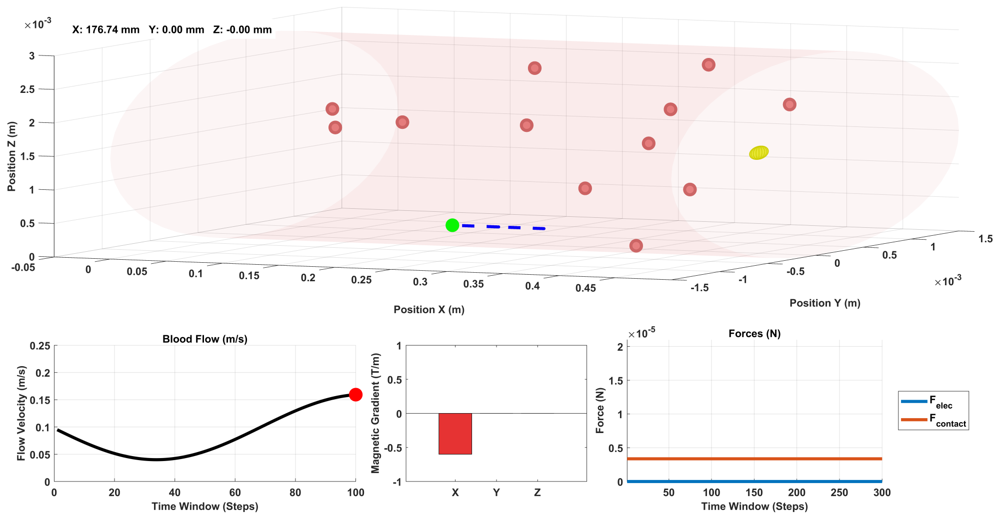

(b) Upstream navigation against hydrodynamic drag using negative X-axis magnetic gradients.

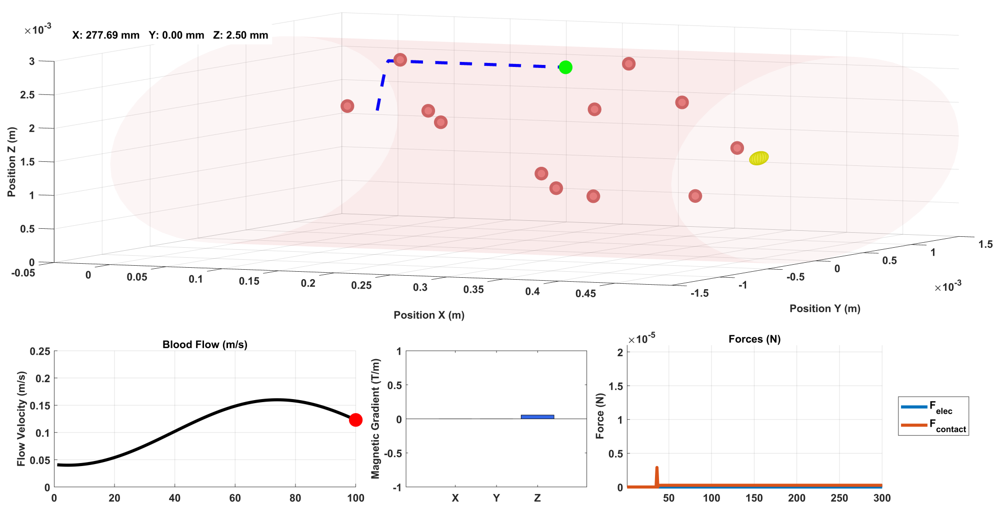

(c) Vertical levitation and gravitational compensation through Z-axis gradient.

Fig. 2: Micro-robot trajectories under different magnetic actuation conditions.

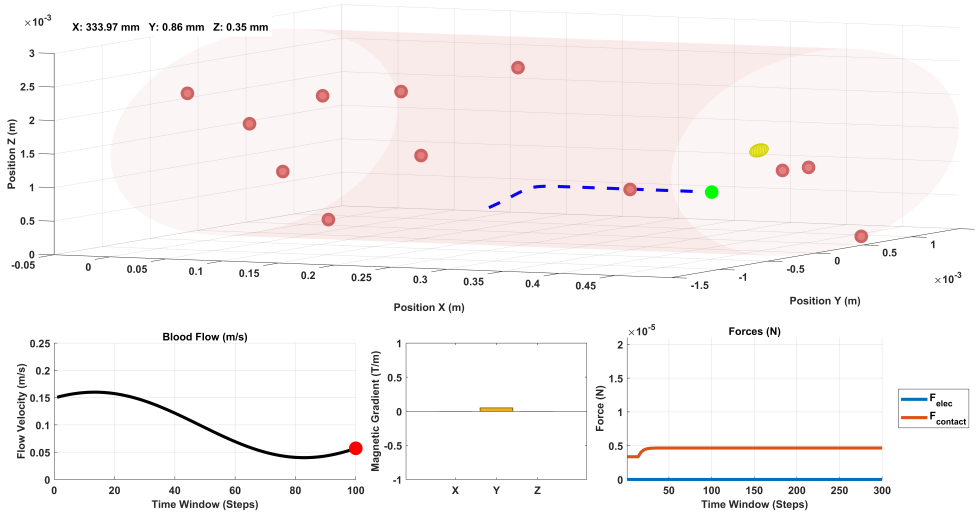

(d) Lateral displacement under Y-axis actuation.

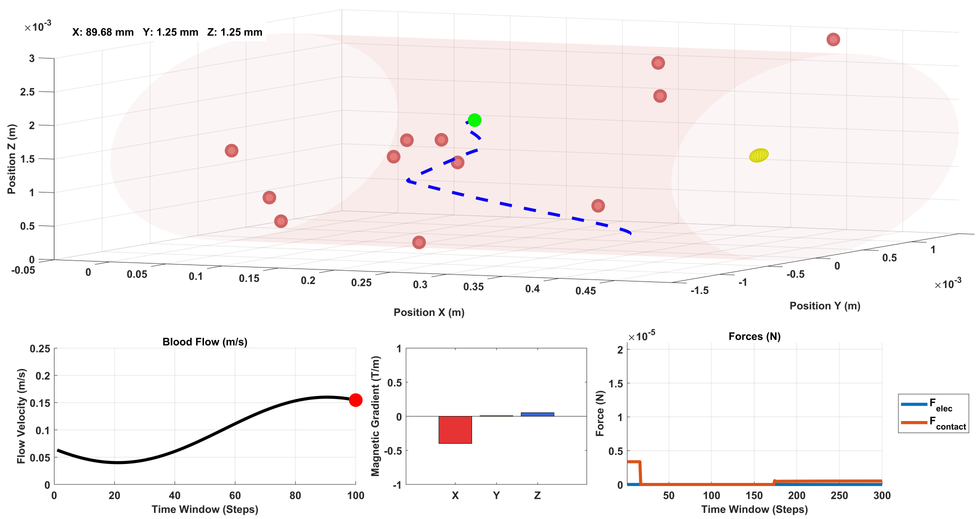

(e) Multiple 3D trajectory using multi-axial gradients.

Fig. 2: (continued)

TABLE I: Parameters used in the simulation

Parameter	Value	Unit	Code	Symbol
Radius of the micro-robot	250×10^{-6}	m	R	r
Density of magnetic material [8]	7500	kg/m^3	rho_mag	ρ_m
Density of polymer matrix [8]	1500	kg/m^3	rho_poly	ρ_{poly}
Density of the fluid (Blood) [9]	1060	kg/m^3	rho_fluido	ρ_f
Dynamic Viscosity (Blood) [9]	0.0035	$Pa \cdot s$	mu	η
Ferromagnetic ratio [8]	0.8	-	tau_m	τ_m
Gravity	9.81	m/s^2	g	g
Saturation Magnetization [10]	1.23×10^6	A/m	M_sat	M_{sat}
Tube diameter	0.003	m	H_tubo	D
Mean speed (Flow)	0.10	m/s	v_media	v_{mean}
Pulse speed amplitude	0.06	m/s	v_pulso	v_{pulse}
Cardiac frequency	1.2	Hz	f_cardiaca	f_c
Net charge [8]	1×10^{-12}	C	q_robot	q
Poisson ratio (Robot)	0.45	-	nu_r	ν_r
Poisson ratio (Wall) [11]	0.5	-	nu_w	ν_w
Young's Modulus (Robot)	1×10^6	Pa	E_r	E_r
Young's Modulus (Wall) [11]	0.5×10^6	Pa	E_w	E_w
Unload exponent	1.5	-	p_exp	p

recording data in double-precision floating-point format.

A high sampling frequency of 5 kHz ($dt = 0.0002$ s) was selected to ensure the numerical stability of the Runge-Kutta (RK4) integration. The non-linear nature of the Hertzian contact mechanics results in highly stiff differential equations during collisions. Lower sampling rates would fail to capture the micro-second dynamics of the impact.

During operated navigation, the system dynamically records the environment dynamics as Markov Decision Process (MDP) state-action-reward tuples:

$$(S_t, A_t, R_t)$$

The state vector S_t encapsulates the micro-robot's 3D kinematics and the instantaneous pulsatile hemodynamic velocity, while the action vector A_t records the applied multi-axial magnetic gradients. The exported dataset comprises 12 features per time step:

$$[t,\ x,\ y,\ z,\ v_x,\ v_y,\ v_z,\ v_{fluid},\ \nabla B_x,\ \nabla B_y,\ \nabla B_z,\ R_t]$$

A real-time dense reward function R_t was implemented to evaluate the agent's performance. The function rewards spatial progression towards a theoretical target while applying penalties when Hertzian contact forces ($||\vec{F}_c|| > 0$) against the arterial walls are detected. The reward logic is defined as:

$$R_t = \begin{cases} 5000\,\Delta d - 10^6\|\vec{F}_c\| + 5000, & d_{\text{target}} < 5 \times 10^{-4}\,\text{m} \\ 5000\,\Delta d - 10^6\|\vec{F}_c\|, & \text{otherwise} \end{cases} \tag{26}$$

Where Δd represents the reduction in Euclidean distance to the target compared to the previous time step, and d_{target} is the absolute distance to the target. This architecture successfully generates datasets comprising hundreds of thousands of state transitions, bypassing the need for computationally prohibitive online simulator interactions.

This data is extracted and saved, when the exportation button is clicked, into a `.csv` to be used in subsequent works.

F. Dataset Extraction Example

To validate the reward structure, Table II presents a truncated excerpt (rounded to five decimal places) of a generated dataset, with a theoretical target positioned at $(0.45,\ 0.0,\ 0.0015)$ meters.

The first example illustrates an undesired manoeuvre: the micro-robot moves out of range in the Y-axis and collides with the vessel boundary. The slight negative Y position indicates the indentation depth into the soft tissue, accurately captured by the contact mechanics model. Despite making marginal forward progress, the system correctly assigns a massive negative reward due to the collision.

The second example demonstrates a safe navigation step. The agent applies Y and Z gradients without triggering contact forces, resulting in a positive reward proportional to its target approach.

Finally, the third example depicts the terminal state where the micro-robot successfully reaches the target radius ($d_{target} < 0.0005$ m), triggering the predefined 5000-point terminal bonus.

G. Future AI Implementation Framework

The structured generation of high-fidelity physical data establishes a direct pipeline for advanced Machine Learning applications. Traditional Online Reinforcement Learning is often unfeasible for complex biomechanical simulations due to the massive computational requirements of calculating hydrodynamics and Hertzian contact at every step. [12]

Instead, the exported MDP tuples will serve as the foundation for Offline Reinforcement Learning and Imitation Learning architectures. Models such as Conservative Q-Learning (CQL) [13] or Decision Transformers [14] can receive this pre-recorded data to learn optimal control policies without interacting directly with the ODE solver.

Once the neural network successfully learns to map states (S_t) to optimal gradients (A_t) maximizing the expected return, the lightweight trained policy can be deployed back into the MATLAB environment (or a physical electromagnetic control system) to achieve real-time, autonomous endovascular navigation, and fine-tune neural networks with Online Reinforcement Learning

VI. Social Impact

Beyond the physical and computational advancements, this framework carries significant implications for the democratization of cardiovascular care. Currently, endovascular interventions require highly specialized infrastructure (such as catheterization laboratories), extensive surgical training, and expose both patients and medical staff

TABLE II: Extract from the teleoperated navigation dataset (values rounded to 5 decimal places)

		State Tuple (S_t)							**Action Tuple (A_t)**			**Reward**
Ex.	t	x	y	z	v_x	v_y	v_z	v_{fluid}	∇B_x	∇B_y	∇B_z	R_t
1	28.43000	0.11604	-0.00128	0.00151	0.11879	-0.12894	-0.00056	0.13996	0.00000	-0.30000	0.05324	-1462.16885
2	29.33440	0.22677	0.00066	0.00157	0.21537	-0.19283	0.00074	0.15721	0.00000	-0.30000	0.05324	0.21647
3	20.91280	0.44963	0.00000	0.00181	0.12599	0.00000	0.00306	0.13384	0.00000	0.00000	0.05324	5000.09691

to harmful radiation from prolonged X-ray fluoroscopy.

Furthermore, traditional intravenous thrombolytic therapies using drugs like recombinant tissue plasminogen activator (rtPA) are severely constrained by a narrow therapeutic "golden window", typically limited to 3 to 4.5 hours from the first symptoms. If a patient is located in a remote or underserved region, the time required for transportation to a centralized neurovascular hub often disqualifies them from receiving these critical, life-saving treatments.

By enabling the precise, wireless navigation of microrobots, this technology has the potential to drastically reduce procedural times, lower hospital costs, and minimize systemic side effects associated with high-dose intravenous drugs by delivering concentrated payloads directly to the occlusion.

More importantly, the transition towards teleoperated, and eventually autonomous, micro-surgery aligns with the urgent need for equitable healthcare innovation. By decoupling the expert surgeon's physical presence from the operating room, this framework facilitates remote, rapid access to targeted therapies like active thrombolysis. Ultimately, this approach bridges the geographical healthcare inequality gap and directly addresses the time-critical nature of thrombotic emergencies across the Americas.

VII. Conclusion and Future Work

This research successfully established a physics-informed computational framework for the study of magnetic microrobot dynamics in vascular environments. By integrating a mathematical model that accounts for both long-range magnetic actuation and short-range contact mechanics, a highly realistic platform for evaluating endovascular navigation strategies was developed.

The interactive MATLAB simulation proved effective in replicating the challenges of navigating against pulsatile blood flow while maintaining numerical stability through hybrid drag models. Advancing beyond a purely physical simulation, this work bridged the critical gap toward AI-driven autonomy by implementing a real-time data extraction architecture. By exporting state-action-reward tuples (S_t, A_t, R_t) during teleoperation, the system saves the computational costs typically associated with training algorithms in complex biomechanical environments.

The generation of these datasets provides a robust and immediate foundation for future work, which will focus on training Imitation Learning and Offline Reinforcement Learning architectures (such as Decision Transformers or Conservative Q-Learning) to optimize trajectory planning.

Ultimately, the fusion of physics-informed biomechanics and Artificial Intelligence presented in this study lays the vital groundwork for a future where autonomous micro-robots navigate the human vasculature with unprecedented precision, transforming endovascular interventions from highly invasive, centralized procedures into accessible, automated therapies that safeguard human life.

Simplifying the vascular geometry to a straight cylinder is a limitation of this initial framework, as real endovascular procedures involve complex anatomies with bifurcations, curvatures, and varying diameters. However, building upon this proof of concept, our ongoing work has already successfully extended this simulation environment to integrate realistic vascular geometries. The navigation challenges and RL datasets derived from these complex anatomies will be the focus of our upcoming work.

References

[1] A. Agrawal, R. Soni, D. Gupta, and G. Dubey, "The role of robotics in medical science: Advancements, applications, and future directions," *Journal of Autonomous Intelligence*, vol. 7, no. 3, 2024. [Online]. Available: https://doi.org/10.32629/jai.v7i3.1008

[2] P. E. Dupont, "A decade retrospective of medical robotics research from 2010 to 2020," *Science Robotics*, 2021.

[3] Y. Shao, A. Fahmy, M. Li, C. Li, W. Zhao, and J. Sienz, "Study on magnetic control systems of micro-robots," *Frontiers in Neuroscience*, vol. 15, p. 736730, 2021. [Online]. Available: https://doi.org/10.3389/fnins.2021.736730

[4] F. C. Landers, L. Hertle, V. Pustovalov, D. Sivakumaran, C. M. Oral, O. Brinkmann, K. Meiners, P. Theiler, V. Gantenbein, A. Veciana, M. Mattmann, S. Riss, S. Gervasoni, C. Chautems, H. Ye, S. Sevim, A. D. Flouris, J. Puigmartí-Luis, T. S. Mayor, P. Alves, T. Lühmann, X. Chen, N. Ochsenbein, U. Moehrlen, T. Schubert, Z. Kulcsar, P. Gruber, M. Weisskopf, Q. Boehler, S. Pané, and B. J. Nelson, "Clinically ready magnetic microrobots for targeted therapies," *Science*, vol. 390, no. 6774, pp. 710–715, 2025. [Online]. Available: https://www.science.org/doi/abs/10.1126/science.adx1708

[5] D. Sun, W. Gao, H. Hu, and S. Zhou, "Why 90% of clinical drug development fails and how to improve it?" *Acta Pharm Sin B*, 2022.

[6] A. Salehi, S. Hosseinpour, N. Tabatabaei, M. S. Firouz, N. Zadebana, R. Nauber, and M. Medina-Sánchez, "Advancements in machine learning for microrobotics in biomedicine," *Advanced Intelligent Systems*, vol. 6, no. 10, p. 2400458, 2024.

[7] H. Shen, S. Cai, Z. Wang, Z. Ge, and W. Yang, "Magnetically driven microrobots: Recent progress and future development," *Materials Design*, vol. 227, p. 111735, 2023. [Online]. Available: https://www.sciencedirect.com/science/article/pii/S0264127523001508

[8] P. E. Dupont, "Adaptive controller and observer for a magnetic microrobot," *IEEE Transactions on Robotics*, 2013.

[9] J. D. Cutnell and K. W. Johnson, *Physics*, 4th ed. Wiley, 1998, p. 308.

[10] J. M. D. Coey, *Magnetism and Magnetic Materials*. Cambridge: Cambridge University Press, 2010, p. 409.

[11] G. A. Holzapfel, "Biomechanics of soft tissue," in *Handbook of Materials Behavior*, J. Lemaitre, Ed. San Diego: Academic Press, 2001, pp. 1057–1071.

[12] S. Sujit, P. H. M. Braga, J. Bornschein, and S. E. Kahou, "Bridging the gap between offline and online reinforcement learning evaluation methodologies," 2023. [Online]. Available: https://arxiv.org/abs/2212.08131

[13] A. Kumar, A. Zhou, G. Tucker, and S. Levine, "Conservative q-learning for offline reinforcement learning," in *Advances in Neural Information Processing Systems (NeurIPS)*, vol. 33, 2020, pp. 1179–1191.

[14] L. Chen, K. Lu, A. Rajeswaran, K. Lee, A. Grover, M. Laskin, P. Abbeel, A. Srinivas, and I. Mordatch, "Decision transformer: Reinforcement learning via sequence modeling," in *Advances in Neural Information Processing Systems (NeurIPS)*, vol. 34, 2021, pp. 15 084–15 097.